Soft Matter

PAPER

View Article Online
View Journal | View Issue

Cite this: *Soft Matter*, 2025, **21**, 1571

Fine-tuning the architecture of microgels by varying the initiator addition time†

Elena Buratti, ‡[a] Fabrizio Camerin, ‡[b] Valentina Nigro, [c] Silvia Franco, [de] José Ruiz-Franco, [fg] Lionel Porcar, [h] Roberta Angelini, [de] Barbara Ruzicka, [de] Yuri Gerelli [de] and Emanuela Zaccarelli *[de]

Received 12th October 2024,
Accepted 19th January 2025

DOI: 10.1039/d4sm01200c

rsc.li/soft-matter-journal

Poly-*N*-isopropylacrylamide (PNIPAM) microgels are versatile colloidal-scale polymer networks that exhibit unique responsiveness to external stimuli, such as temperature. While the synthesis of PNIPAM microgels is well-documented, there is limited exploration of how their structural properties can be modified by subtle changes in the polymerization process. In this work, we carefully investigate how varying the time of addition of a common initiator, such as potassium persulfate, during the polymerization process allows a precise control over microgel architecture. Our findings, based on a combination of numerical simulations, scattering, and rheology experiments, reveal that delayed initiator addition results in a more heterogeneous network, characterized by a less extended corona. In contrast, more homogeneous microgels are obtained by adding the initiator all at the start of the synthesis. In this way, the internal mass distribution of the particles can be tuned, highlighting the importance of synthesis timing for optimizing microgel conformation and functionality in tailored applications.

1 Introduction

Microgels are colloidal-scale polymer networks that represent the prototype model system for soft repulsive particles.[1–4] Their ability to respond to external control parameters, such as temperature in the case of the widely investigated poly-*N*-isopropylacrylamide (PNIPAM), makes them very valuable for a wide range of applications,[5,6] from nanosensing[7] to biomedicine.[8]

The experimental synthesis of PNIPAM microgels is well-documented in the literature[9,10] and follows a general recipe, that is used by the large majority of the research groups worldwide. It is well-known that such a synthesis protocol gives rise to polymer networks, that are not homogeneous. Rather, they are characterized by a so-called core–corona structure, due to the fact that crosslinkers, usually *N*,*N*-methylenebisacrylamide (BIS) molecules, react significantly faster than NIPAM monomers in the polymerization process. In this way, microgels comprise a denser, inner part that is richer in crosslinkers (the core), and a fluffier, external shell (the corona), where only few crosslinkers are present. This characteristic structure has been revealed by neutron and X-ray small-angle scattering experiments at high dilution, measuring the microgels form factors, that are well-described by the celebrated fuzzy sphere model.[11,12]

The synthesis protocol can also be adapted to modify the overall internal conformation of the particles. To this aim, some studies have focused on the possibility to obtain more homogeneous microgels. This can either be achieved by starting with oligomers rather than monomers in the reaction batch[13] or *via* continuous monomer feeding.[14] Another possibility is to act on the initiator of the polymerization process. However, no specific differences in structure or swelling properties have been reported if different types of initiators, such as potassium persulfate (KPS) or ammonium persulfate (APS), were employed.[15,16] Similarly, for anionic or cationic initiators

[a] *Department of Chemical, Pharmaceutical and Agricultural Sciences, University of Ferrara, via L. Borsari 46, 44121 Ferrara, Italy*
[b] *Physical Chemistry, Department of Chemistry, Lund University, SE-22100 Lund, Sweden*
[c] *Photonics Micro and Nanostructures Laboratory, Nuclear Department, ENEA Frascati Research Centre, Via E. Fermi 45, 00044 Frascati, Italy*
[d] *Italian National Research Council, Institute for Complex Systems (CNR-ISC), Sapienza University of Rome, Piazzale Aldo Moro 5, 00185 Rome, Italy. E-mail: emanuela.zaccarelli@cnr.it*
[e] *Department of Physics, Sapienza University of Rome, P.le A. Moro 2, 00185 Roma, Italy*
[f] *Department of Condensed Matter Physics, University of Barcelona, Carrer de Martí i Franqués 1, Barcelona 08028, Spain*
[g] *Institute of Complex Systems (UBICS), University of Barcelona, Carrer de Martí i Franqués 1, Barcelona, 08028, Spain*
[h] *Institut Laue-Langevin, 71 avenue des Martyrs, Grenoble 38000, France*

† Electronic supplementary information (ESI) available: Experimental, model, and numerical form factors for the surfactant-free sample together with tables summarising the main structural parameters derived from the analysis of SANS data for all investigated samples. Parameters related to the analysis of DLS data according to the modified cumulant expansion method. See DOI: https://doi.org/10.1039/d4sm01200c

‡ These authors contributed equally to this work.

like 2,2-azobis(2-methylpropionamidine) dihydrochloride (AIBA), it was shown that the microgel properties are largely unaffected.[17]

Nevertheless, a less investigated aspect is the addition time of the initiator, which is typically introduced into the reaction batch either in a single shot or in a controlled way within a fixed amount of time. This subtle change in the protocol could have non-trivial effects on the resulting particles, since one could expect that a drop-by-drop addition would create more nuclei, leading to smaller microgels, as compared to a one-time addition that could form a lower number of polymerization centers. In addition to size modifications, the initiator time could also favor a different internal organization of crosslinkers and monomers, thus affecting the features of the core–corona structure. Expectations would be in favor of more homogeneous microgels with a more controlled drop-by-drop addition, while a more heterogeneous structure could be expected with the initiator being added altogether.

In this work, we aim to systematically explore this effect by preparing microgels with different amounts of initiator time t_{add}, leaving unaltered all the other parameters in the synthesis. The parameter t_{add} represents the duration of the continuos feeding of the KPS initiator, ranging from t_{add} = 0.2 min, where all KPS is added at the same time, up to t_{add} = 9 min, where KPS is added at an approximate rate of 0.27 mM min^{-1}. The microgels hydrodynamic size and internal structure are determined by means of dynamic light scattering (DLS) and small angle neutron scattering (SANS) techniques, respectively. To interpret the results, we rely on computer simulations based on a monomer-resolved microgel model, recently established in our group,[12,18] which was shown to be able to capture the internal structure of microgels at different crosslinker concentration.[19] To capture the subtle variation of the structure with different initiator addition times, we slightly modify our *in silico* assembly procedure to account for modifications of the core–corona ratio within the particles. The microgel modeling is further aided by rheological measurements from which we extracted relevant information on the number of polymerization nuclei in the reaction batch. In this way, we are able to fully describe the observed experimental variations given by the addition of KPS from t_{add} = 0.2 min up to t_{add} = 9 min.

Our findings reveal interesting features for the obtained microgels. Specifically, we find that when the initiator is added during a very short time interval, polymerization occurs on few nuclei in the reaction batch, following our initial expectations, giving rise to overall larger microgels. At the same time, such particles present a quite extended core with respect to the total size of the microgels and thus a more homogeneous structure. On the contrary, our analysis evidences the tendency for the formation of smaller particles when initiator is included within longer times. This is related to the possibility of creating multiple polymerization centers over time so that, at fixed amount of added monomer, the particles have a smaller hydrodynamic radius. In the latter case, crosslinkers are more confined within the inner part of the microgels, resulting in a more heterogeneous structure with a smaller core as compared to the former scenario. The interpretation of the experimental results, which only show a moderate variation with increasing addition time, is facilitated by the adopted simulations. These complement the measurements by offering an insightful microscopic perspective.

Overall, these results provide a better understanding of the processes taking place during the experimental synthesis, and offer a guide on how to leverage the initiator addition time for obtaining microgels with different sizes and architectures.

2 Materials and methods

2.1 Experimental section

2.1.1 Reagents. *N*-Isopropylacrylamide (NIPAM) (Sigma-Aldrich, St. Louis, MO, USA), purity 97%, was purified by recrystallization from hexane, dried under reduced pressure (0.01 mmHg) at room temperature and stored at 253 K. *N*,*N*-Methylenebisacrylamide (BIS) (Sigma-Aldrich, St. Louis, MO, USA), electrophoresis grade, was purified by recrystallization from methanol, dried under reduced pressure (0.01 mmHg) at room temperature and stored at 253 K. Sodium dodecyl sulphate (SDS), purity 98% and potassium persulfate (KPS), purity 98% were purchased from Sigma-Aldrich (St. Louis, MO, USA) and used as received. Ultrapure water (resistivity: 18.2 MW cm^{-1} at room temperature) was obtained with Arium pro Ultrapure water purification Systems, (Sartorius Stedim Biotech SA, DE). All the other solvents (Sigma Aldrich RP grade) were used as received. Dialysis membrane, SpectraPor 1, MWCO 6–8 kDa (Spectrum Laboratories, Inc., Piscataway, NJ, USA) was soaked in distilled water for 2 h and then thoroughly rinsed before use.

2.1.2 Microgel synthesis. Several PNIPAM microgels were synthesised using the same conditions for the precipitation polymerization, but changing the addition time of the initiator. In particular, NIPAM (0.137 M), BIS (1.87 mM) and SDS (0.17 mM) were solubilized in 230 mL of ultrapure water into a 250 mL jacket reactor. The solution was deoxygenated by bubbling nitrogen for 1 h and then heated at 343 K. Initiator KPS (2.44 mM) was dissolved in 10 mL deoxygenated water and added to initiate the polymerization. The addition was performed with a syringe pump, dropping the same amount of solution in five different times (0.2, 0.5, 1, 4 and 9 min), in order to obtain five different PNIPAM samples. Then, for each sample, the reaction was left to proceed for 4 h. The crude dispersions were purified by dialysis (MWCO 6–8 kDa) with distilled water with frequent water change for 2 weeks, they were recovered and the microgel concentrations were calculated by gravimetric analysis to be 1.3 ± 0.1 wt% for each sample. In addition, to assess size effects of the present results, we also synthesised microgels with the same amounts of NIPAM and BIS in the absence of surfactant. In this case, the addition time was 9 minutes only.

2.1.3 Dynamic light scattering. DLS measurements were performed on PNIPAM microgels in H_2O at concentration of 0.01% by weight and at temperatures ranging from 293 K to 313 K, with a 2 K temperature step. Measurements were carried out using polarized monochromatic incident laser beam with

wavelength λ = 642 nm. Scattered photons were collected, by a single mode collecting fiber, at 90° scattering angle and the resulting information was expressed in terms of intensity auto-correlation function, $g_2(t)$. The latter was analysed using a stretched exponential function as $g_2(t) = 1 + b[e^{-(t/\tau)\beta}]^2$, where τ is the relaxation time, β the stretching exponent and b a scaling factor. If $\beta \approx 1$, as in the case of all the samples investigated in the current work, the solution can be considered monodisperse and τ represents the average relaxation time. An alternative modeling approach, namely the modified cumulant method,[20] was also applied to the data to ensure the robustness of the analysis. As detailed in the ESI,† the parameters obtained from this method confirmed that the samples can be considered monodisperse, with no significant deviations observed compared to the results from the stretched exponential model. The hydrodynamic radius of the particles can be then derived through the Stokes–Einstein relation as $R_H = k_B T/6\pi\eta D_t$, where k_B is the Boltzmann constant, η the viscosity of water and D_t the translational diffusion coefficient of the microgel particles. The latter is related to the relaxation time τ through the relation $\tau = 1/(q^2 D_t)$, where $q = 1.84 \times 10^{-3}$ Å^{-1} in the present case. For all investigated samples, this q value is far from any minima of the form factor, leading to a scattered intensity sufficiently high to ensure an adequate signal-to-noise ratio.

2.1.4 Small angle neutron scattering. SANS experiments were carried out at the Institut Laue-Langevin (ILL, Grenoble, France) using the D22 small-angle diffractometer. The instrument was equipped with two detectors, a front one, fixed at 1.4 m from the sample position and a rear one that was placed at two distances, namely 5.6 m and 17.6 m from the sample position. By using two incident wavelengths, namely λ = 6 Å (for the 5.6 m configuration) and λ = 11.5 Å (for the 17.6 m configuration, with no beam-stopper) it was possible to collect data in a q-range from 9.4×10^{-3} Å^{-1} to 0.68 Å^{-1}. In these configurations, the instrumental resolution, usually reported as $\Delta q/q$ ranged from ≈20% for the lowest q-values down to ≈4% at high qs. In order to better resolve the sharp features expected in the experimental data, the beam aperture was reduced to 10 mm diameter. Microgel dispersions were prepared as described for DLS experiments but at a 0.3% weight concentration and using D_2O instead of H_2O as dispersing medium to enhance the scattering signal from the polymer and reduce the incoherent background level.[21] SANS measurements were performed on samples prepared with KPS added in 0.2, 1 and 9 minutes as well as for the surfactant-free samples with KPS added in 9 minutes. Samples were placed in quartz cuvettes (Hellma, Germany) with 2 mm path length. Cuvettes were then loaded in a multi-position thermostated rack. Measurements were performed at 293 K and 313 K.

For each sample, the scattering intensity $I(q)$ was obtained from the radial averaging of the 2-D detector images using the GRASP[22] software. Absolute scattering units (*i.e.* cm^{-1}) normalisation was achieved by accounting for the measured neutron flux and for the sample and empty cell transmission values.

Experimental data acquired for the empty cell and for the pure D_2O were subtracted from those of the sample to the data analysis, which was then performed using the SasView software.[23] SANS intensity *versus* q curves were analyzed using a model based on the fuzzy sphere form-factor.[11] This model includes the fuzzy-sphere form factor $P_{inho}(q)$ (eqn (1)), the gel network density fluctuations contribution $P_{fluct}(q)$ (eqn (2)) and a flat, q-independent, background (*bkg*).

In detail, the fuzzy-sphere form-factor was expressed as[11]

$$P_{inho}(q) = \left(SLD_p - SLD_s\right)^2 \left[\frac{3[\sin(qR) - qR\cos(qR)]}{(qR)^3} \exp\left(-\frac{(\sigma_f q)^2}{2}\right)\right]^2 \quad (1)$$

where SLD_p–SLD_s is the contrast term[21] (*i.e.*, the difference between the scattering length density of the polymer, SLD_p, and that of D_2O, SLD_s). Such a model corresponds to a radial density profile featuring a core–corona architecture, with a polymer-rich core and a less dense spanning corona. In analogy with the definitions used in the numerical simulations reported in the present work, R represents the particle core radius, and $R + 2\sigma_f$ represents the total particle radius, where σ_f is the width of the smeared particle surface. These quantities are the experimental counterparts of C and Z, as defined in the numerical section.

It is worth noticing that for $\sigma_f = 0$, $P_{inho}(q)$ corresponds to the form-factor of a homogeneous spherical particle of radius R.

The gel network contribution was modeled using a Lorentzian function

$$P_{fluct}(q) = \frac{1}{1 + \xi^2 q^2}, \quad (2)$$

where ξ is the correlation length of the density fluctuations. This contribution is absent for particles in the collapsed state, as the gel network becomes too compact to be resolved in SANS experiments. The expression for the total theoretical scattering intensity was

$$I_m(q) = c \cdot P_{inho}(q) + I_{fluct}(0) \cdot P_{fluct}(q) + bkg \quad (3)$$

where c is the particle number density, $I_{fluct}(0)$ is the scattering intensity at q = 0 for the Lorentzian component, and *bkg* corresponds to the incoherent $q-$ independent background signal. Finally, the expression for $I_m(q)$ (eqn (3)) was convoluted with the instrumental resolution, $R(q)$, provided as part of the data reduction step.

$$I(q) = I_m(q) \circledast R(q) \quad (4)$$

The resulting expression (eqn (4)) was fitted to the experimental data using a least-squares minimization method. This procedure led to the determination of R, σ_f, ξ, c, $I_{fluct}(0)$, and *bkg*. Importantly, this model does not include any polydispersity function to account for size variations, thus assuming a monodisperse particle population.

2.1.5 Rheology. Rheological measurements were performed using a stress-controlled rotational rheometer Anton Paar MCR102 equipped with a cone-plate geometry. The plate has 24.964 mm diameter, 1.998° cone angle and 104 μm truncation.

Temperature control was maintained using a Peltier system, and solvent evaporation was prevented by saturating the atmosphere surrounding the sample with water and by using an evaporation blocker around the plate and an isolation hood. Before each measurement, samples were pre-sheared at a shear rate of $\dot{\gamma}$ = 500 s^{-1} for 30 seconds to obtain a reproducible initial state by erasing any previous mechanical history. After loading, the sample was allowed to equilibrate thermally for a few minutes before starting the measurement. The flow curves of viscosity as a function of shear rate are described by means of the Cross model:[24]

$$\eta = \eta_\infty + \frac{\eta_0 - \eta_\infty}{1 + (\dot{\gamma}/\dot{\gamma}_c)^m} \quad (5)$$

where η_0 and η_∞ represent the limiting viscosity at zero and infinite shear rates, respectively, while $\dot{\gamma}_c$ is a critical shear rate and m is a positive power exponent. To estimate an effective packing fraction ϕ_{eff}, viscosity measurements were performed in dilute conditions as a function of the weight concentration C_w. Specifically, the dependence of the relative viscosity $\eta_r = \eta/\eta_s$, with η_s the solvent viscosity in the absence of the microgels, on the packing fraction ϕ_{eff} is given at low concentrations by the Einstein–Batchelor equation:[25]

$$\eta_r(\phi_{eff}) = 1 + 2.5\phi_{eff} + 5.9\phi_{eff}^2. \quad (6)$$

Here, we use the linear relation $\phi_{eff} = kC_w$ to convert weight concentration into packing fraction, following previous works.[26,27] In this way, we can estimate the shift parameter k that depends on the specific microgel considered. Indeed, this parameter expresses how microgels of different internal architecture correspond to different occupied volumes, and thus different effective packing fractions.

2.2 Numerical section

2.2.1 *In silico* microgel assembly. The microgel polymer network is assembled in a spherical confinement of radius Z, starting from N patchy particles of diameter σ and mass m (the units of length and mass in simulations, respectively) with valence two and four, which mimic respectively the connectivity of monomers and crosslinkers in standard PNIPAM microgels. Assembly simulations are performed for with the oxDNA simulation package on GPUs[28] until almost the totality of possible bonds (>99.9%) are formed. Details on interaction potentials and parameters used for the assembly can be found in ref. 18. In addition, the assembly is carried out in the presence of a radial force that acts on particles with valence four,[12] which allows to tune their position within the network, thus resembling the different reactivity of crosslinkers as compared to monomers. The designing force reads as

$$\vec{f_d} = \begin{cases} -kr\hat{r} & \text{if } 0 < r \leq C \\ -g\hat{r} & \text{if } C < r < Z, \end{cases} \quad (7)$$

with $C < Z$ an intermediate length within which crosslinkers are mostly confined, and $k = 4.5 \times 10^{-5}$ and $g = 0.008$ two phenomenological constants.[12] For a given N, Z is also fixed in such a way that the monomer number density ρ_{mon} remains constant. Hence, we always ensure that

$$\rho_{mon} = \frac{3}{4\pi}\frac{N}{Z^3} \simeq 0.08\sigma^{-3}, \quad (8)$$

whose value was validated against experiments at different crosslinker concentrations.[12,19]

In this work, for capturing the dependence on the initiator addition time t_{add}, we introduce a few differences with respect to this previously established assembly protocol. First of all, we change the value of C with respect to Z in order to vary the confinement of the crosslinkers. Secondly, we act on the short-time (bare) diffusion coefficient D_0 of the Brownian thermostat in the simulations used for the assembly. In fact, we observed that by setting $D_0 = 0.1\sigma\sqrt{\varepsilon/m}$, as in the previously established method,[12] the results were rather independent of C. The use of $D_0 = 1.0\sigma\sqrt{\varepsilon/m}$ appears to fix this issue. For consistency, we note that the method put forward in ref. 12 with $C = Z/2$ and $D_0 = 0.1\sigma\sqrt{\varepsilon/m}$ yields statistically identical assembly results to the case where $C = 0.65Z$ and $D_0 = 1.0\sigma\sqrt{\varepsilon/m}$ reported in this work. This choice, as shown below, corresponds to the experimental case t_{add} = 9 minutes.

In addition, in order to be consistent with rheological measurements, which provide indirect information on the packing fractions of the different samples, as discussed in detail below, we also vary the number of monomers N, and thus Z, ensuring the validity of eqn (8). For convenience, all relevant assembly parameters for the microgels discussed in the present work are summarized in Table 1, together with the assigned names to the samples. In this respect, the subscript refers to the size of the microgel based on the number of particles (s = small, m = medium, l = large), while the apex, where present, is related to the size of the spherical region defined by C, that is roughly the core radius. We note that the experimental value of t_{add} is not present for the cases that cannot be directly compared to experiments, due to the lack of neutron scattering and viscosity measurements for the intermediate samples.

2.2.2 Coarse-grained bead-spring microgel model. Once the networks are assembled, the interactions between all monomers are based on the well-established bead-spring model. Beads interact *via* a Weeks–Chandler–Anderson (WCA)

Table 1 Parameters for the assembly of *in silico* microgels, reporting microgel given names, corresponding experimental initiator addition time t_{add}, initial number of monomers N in the assembly, core radius C, overall spherical microgel confinement Z, and the core-to-microgel assembly ratio C/Z

Name	t_{add} [min]	N	C [σ]	Z [σ]	C/Z
M_s	9.0	168k	51.6	79.4	0.65
M_m	1.0	230k	66.1	88.1	0.75
M_l^{c50}	—	336k	50	100	0.50
M_l^{c60}	—	336k	60	100	0.60
M_l^{c70}	—	336k	70	100	0.70
M_l	0.2	336k	80	100	0.80

potential[29]

$$V_{\mathrm{WCA}}(r) = \begin{cases} 4\varepsilon\left[\left(\frac{\sigma}{r}\right)^{12} - \left(\frac{\sigma}{r}\right)^{6}\right] + \varepsilon & \text{if } r \le 2^{\frac{1}{6}}\sigma \\ 0 & \text{otherwise,} \end{cases} \quad (9)$$

with ε setting the energy scale and r being the distance between two particles, which is added to the Finitely Extensible Nonlinear Elastic (FENE) potential[30] in case particles are bonded:

$$V_{\mathrm{FENE}}(r) = -\varepsilon k_{\mathrm{F}} R_0^2 \ln\left[1 - \left(\frac{r}{R_0\sigma}\right)^2\right] \quad \text{if } r < R_0\sigma, \quad (10)$$

with $k_{\mathrm{F}} = 15$ determining the stiffness of the bond and $R_0 = 1.5$ the maximum bond distance. To take into account the effect of temperature on the responsiveness of the microgel, we consider an additional solvophobic potential,[31] which mimics the reduced affinity of the monomer to the solvent with increasing temperature, of the following form:

$$V_\alpha(r) = \begin{cases} -\varepsilon\alpha & \text{if } r \le 2^{1/6}\sigma, \\ \frac{1}{2}\alpha\varepsilon\left[\cos\left(\gamma(r/\sigma)^2 + \beta\right) - 1\right] & \text{if } 2^{1/6}\sigma < r < R_0\sigma, \\ & \text{if } r > R_0\sigma. \end{cases} \quad (11)$$

with $\gamma = \pi(2.25\text{–}2^{1/3})^{-1}$, with $\beta = 2\pi - 2.25\gamma$. The V_α potential is modulated by α which controls the strength of the monomer–monomer attractive interactions. For $\alpha = 0$, the microgel is maximally swollen and no attraction in present. Conversely, upon increasing α, the microgel collapses experiencing an effective attraction. Previous works have determined that the volume phase transition occurs at $\alpha \sim 0.65$.[12,18]

2.2.3 Simulations. Molecular dynamics simulations are run in the NVT ensemble ensuring a reduced temperature $T^* = k_{\mathrm{B}}T/\varepsilon = 1$, with k_{B} the Boltzmann constant and T the temperature, by means of a Nosé–Hoover thermostat. Each microgel is placed in the center of a cubic simulation box with side 500σ and periodic boundary conditions. After the assembly, we carry out an equilibration run for at least $1 \times 10^6\delta t$, with $\delta t = 0.002\tau$ and $\tau = \sqrt{m\sigma^2/\varepsilon}$ the unit of time. A subsequent production run is carried out for at least $5 \times 10^6\delta t$. All microgels simulations are performed using the LAMMPS package.[32]

2.2.4 Calculated quantities. In order to compare with experiments, we calculate the numerical form factors as

$$P(q) = \frac{1}{N}\sum_{i,j=1}^{N}\left\langle \exp\left(-i\vec{q}\cdot\vec{r}_{ij}\right)\right\rangle, \quad (12)$$

where r_{ij} is the distance between monomers i and j, while the angular brackets indicate an average over different configurations and over different orientations of the wavevector $\vec{q}$. In real space, we calculate the radial density profiles of the microgel as

$$\rho(r) = \left\langle \frac{1}{N}\sum_{i=1}^{N}\delta(|\vec{r}_i - \vec{r}_{\mathrm{CM}}| - r)\right\rangle. \quad (13)$$

with $\vec{r}_{\mathrm{CM}}$ the distance from the microgel center of mass. Finally, we estimate the hydrodynamic radius of our microgels to compare with DLS measurements, exploiting the method recently put forward in ref. 16. In brief, the hydrodynamic radius is calculated following Hubbard and Douglas as done in ref. 33:

$$R_{\mathrm{H}} = 2\left[\int_0^\infty \frac{1}{\sqrt{(a^2+\theta)(b^2+\theta)(c^2+\theta)}}\mathrm{d}\theta\right]^{-1} \quad (14)$$

where a, b, c are the principal semiaxes of the instantaneous ellipsoid approximating the microgel, calculated through the convex hull of the microgel. This method yields a reliable estimate of R_{H}, that was validated in previous works against experiments.[16,34]

2.2.5 Comparison between SANS data and simulations. The easiest way for comparing our simulations and experiments is to overlap the numerical form factors $P(q)$ with the experimental scattering intensity $I(q)$ by re-scaling the former along the vertical and horizontal axes. However, it is worth recalling that SANS data cannot be directly compared with numerical $P(q)$ due to smearing caused by limited instrumental resolution. Deconvolution of experimental data is possible but not trivial. For this reason, we decided to compare the numerical $P(q)$ with the model $I_{\mathrm{m}}(q)$ (see eqn (3)) resulting from the analysis of the experimental data. Because of the good agreement between model curves and SANS data observed during data analysis, this choice does not pose any issue.

3 Results and discussion

3.1 Experimental characterization

We synthesize five different microgel batches by adding *N*-isopropylacrylamide (NIPAM) as monomer, *N*,*N*-methylenebisacrylamide (BIS) as crosslinking agent, and potassium persulfate (KPS) as initiator of the polymerization process. The five batches differ for the rate of addition of KPS, which is carried out in 0.2, 0.5, 1, 4 and 9 minutes, respectively. The detailed procedure for the microgel synthesis is described in the Methods section.

For characterizing the obtained microgels, we first investigate their hydrodynamic size by DLS. The hydrodynamic radius R_{H} as a function of KPS addition time t_{add} is shown in Fig. 1(a) and (b) at 293 K and as a function of temperature T, respectively. It is clear how the inclusion of the initiator at different times has a strong effect on the overall size of the particles, since R_{H} drops by about 25% if the addition is carried out in less than a minute or in 4 minutes. Smaller differences are instead noted at longer addition times, with R_{H} that changes from 206 to 197 nm for $t_{\mathrm{add}} = 4$ and 9 minutes, respectively.

The response to temperature is typical of other responsive PNIPAM microgels, with a swollen state at low temperatures and a collapsed state at high temperatures. However, we observe a more subtle temperature dependence for different microgel batches. In fact, as shown in Fig. 1(b), different size ranges are explored for different addition times. This is reflected in the overall swelling ratio $\lambda = R_{\mathrm{H}}(T = 293\ \mathrm{K})/R_{\mathrm{H}}(T = 313\ \mathrm{K})$ (see inset in Fig. 1(b)) which goes from about 2.3 for

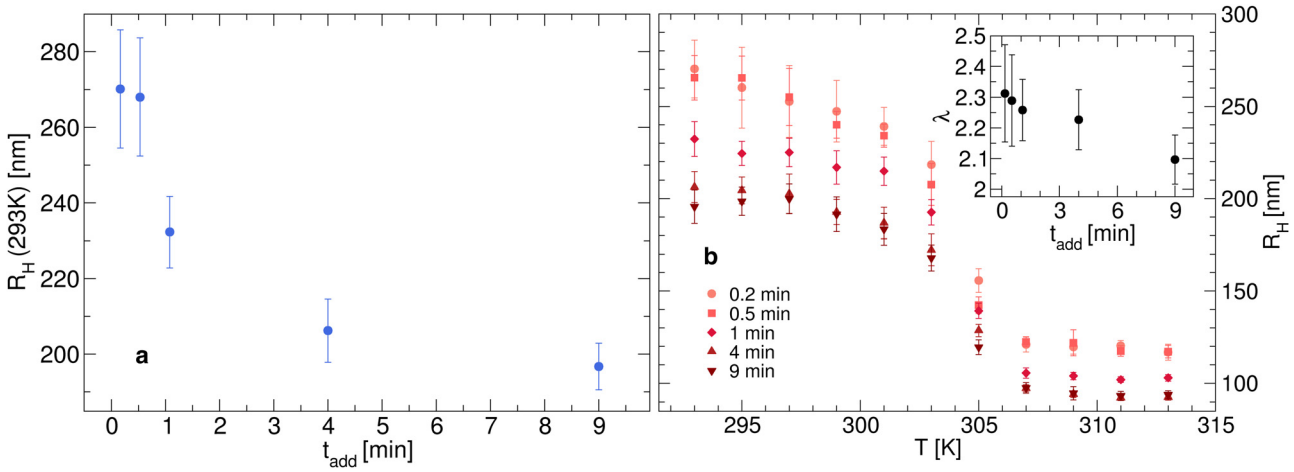

Fig. 1 (a) Hydrodynamic radius R_H for PNIPAM microgels at 293 K as a function of the KPS addition time t_{add}, obtained from DLS measurements on dispersions at concentration of 0.01 wt%. (b) Hydrodynamic radius R_H of PNIPAM microgels as a function of temperature T. In the inset, the swelling ratio λ as a function of the KPS addition time t_{add} is shown.

small t_{add} to about 2.1 when the addition of KPS is carried out for longer times, indicating an increasingly reduced shrinking capability. Despite this, we note that the synthesis procedure does not affect the volume phase transition temperature of the microgels, which remains close to 305 K, as expected.

For three of the five samples we also carry out rheological measurements. The relative viscosity η_{rel} as a function of weight concentration C_w is reported in Fig. 2 for batches with initiator addition time t_{add} = 0.2, 1 and 9 minutes. In all cases we note a similar trend, with the viscosity growing for increasing concentrations. Coherently with expectations, the highest value of viscosity is reached for the sample with t_{add} = 0.2 and with the greatest hydrodynamic radius. As shown in Fig. 2, the relative viscosity data can be fitted by means of eqn (6), which allows us to extract the conversion parameter k, reported in the inset for the three investigated samples. Its decreasing trend as a function of t_{add} is similar to that observed for R_H shown in Fig. 1(a).

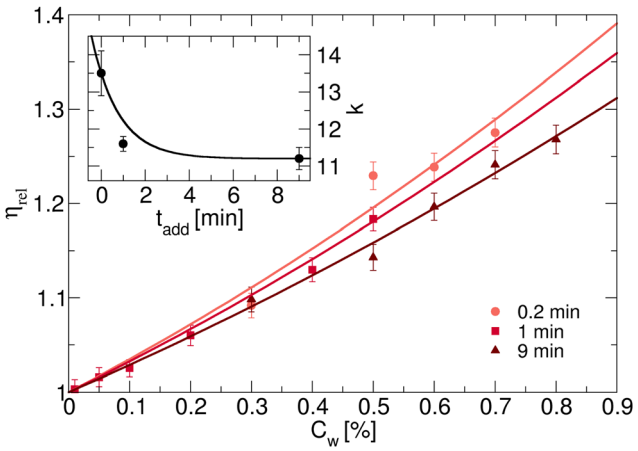

Fig. 2 (a) Relative viscosity η_{rel} for dispersions containing PNIPAM microgels synthesised with KPS added in t_{add} = 0.2,1 and 9 min, as a function of weight concentration C_w. Inset: Shift parameter k, obtained by fitting η_{rel} according to eqn (6). The solid black line is a guide to the eye.

3.1.1 Insights on the microgel structure and morphology by small-angle neutron scattering measurements. We now report the experimental SANS data measured at 293 K and 313 K for microgels synthesised with KPS added in t_{add} = 0.2,1 and 9 min in Fig. 3(a)–(c), respectively. We also show the corresponding best fits obtained using eqn (4) and the "resolution-free" model intensity contributions, $I_m(q)$, computed using eqn (3), *i.e.* without accounting for the instrumental resolution $R(q)$.

As derived from the analysis of the SANS data reported in Fig. 3(a)–(c), in the collapsed state all microgels can be described as homogeneous spheres with a total radius[11] decreasing from 112 ± 3 nm for the sample prepared at t_{add} = 0.2 min to 86 ± 2 nm for the sample prepared at t_{add} = 9 min (Fig. 3(d)). In this model, the fuzziness and the presence of a detectable gel network can be suppressed by setting $\sigma_f = 0$ in eqn (1) and $I_{fluct}(0) = 0$ in eqn (3). At T = 293 K, the microgel form factors are well described by eqn (3). For these swollen microgels, SANS experiments allows us to determine the extension of the corona and that of the core radius, respectively, thanks to the use of the fuzzy sphere model. Also in this case the total radius ($R + 2\sigma_f$) of the particles decreases as the addition time increases. The opposite trend is found for the core–corona ratio, $\frac{R}{R+2\sigma_f}$, shown in Fig. 3(e). Indeed, the extension of the corona, σ_f, is found to be similar for all investigated samples, while larger changes are observed in the extension of the microgel core radius, R. Such decreasing trend in the core–corona ratio reveals that the structure of the microgel gets more heterogeneous as t_{add} increases. For the samples in the swollen state it is also possible to detect the presence of the Lorentzian contribution (eqn (2)) originated by the gel network density fluctuations. Because of the explored q-range, the correlation length ξ could not be determined with high accuracy, resulting ~4 ± 2 nm for all investigated samples.

To assess size effects, we also report form factors measured by SANS for the surfactant-free microgels synthesized with t_{add} = 9 minutes in the ESI.† The results, reported in Fig. S1 (ESI†)

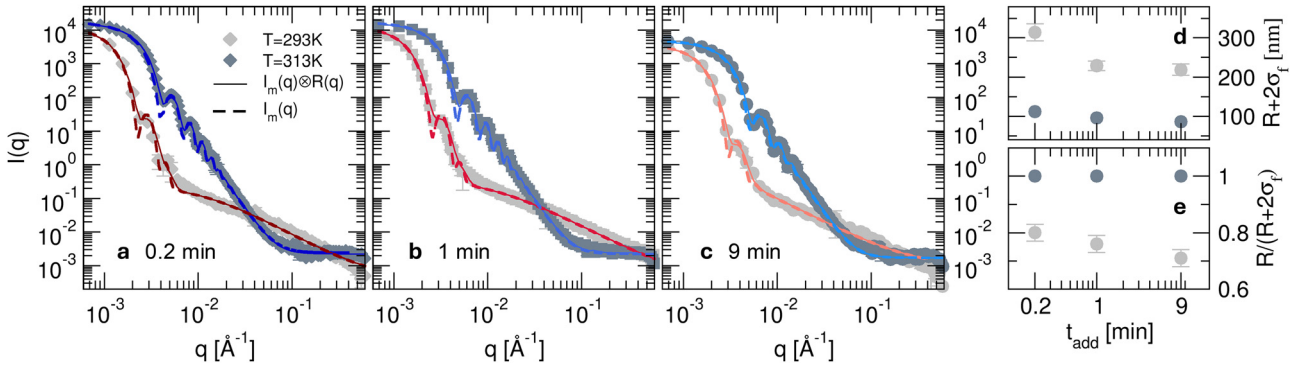

Fig. 3 (a)–(c) Experimental scattering intensity measured on the D22 diffractometer for microgels synthesised in D_2O with KPS added in t_{add} = 0.2, 1 and 9 min in the collapsed (313 K, dark grey symbols) and in the swollen (293 K, light grey symbols) states. Thin solid lines represent the best fits obtained using eqn (4) with the resolution-free $I_m(q)$ curves, shown as thick dashed lines. (d) Total particle radius ($R + 2\sigma_f$) as a function of KPS addition time t_{add} obtained from the fits of the SANS data (panels a–c) for the microgels in the collapsed (313 K, dark grey circles) and in the swollen (293 K, light grey circles) state. (e) Core–corona ratio, $\frac{R}{R+2\sigma_f}$, as a function of the KPS addition time t_{add} obtained from the fits of the SANS data for the microgels for the two analysed temperatures.

are very similar to those of Fig. 3, particularly from the core–corona ratio extracted from the fits and reported for the surfactant-free microgels in Table S1 (ESI†) and for all other samples in Table S2 (ESI†). This indicates that the resulting microgels internal architecture is independent on the amount of added surfactant.

3.2 Establishing a microgel model for describing the role of the initiator addition time t_{add}

Computer simulations represent an important tool for gaining more detailed information on the architecture of the microgels at the single-particle level. *In silico* synthesis in fact allows for a one-to-one comparison with the form factors of the microgel samples measured experimentally, with the advantage of being able to directly study the effect of a change in a parameter on the structure of the particle. In brief, a realistic model for microgels can be obtained by the self-assembly of N patchy particles under spherical confinement in such a way that a crosslinked gel-like structure is obtained. The higher reactivity of crosslinkers compared to monomers, which is typically observed in experiments, can be mimicked by concentrating specific particles in the center of the sphere during assembly by means of an additional designing force $\vec{f}_d$, see eqn (7). Therefore, by applying $\vec{f}_d$ within a radius C, we are able to effectively obtain a more extended or restricted microgel core. Additional details on the microgel assembly are reported in Methods.

It is important to note that the *in silico* synthesis we carry out does not aim to reproduce the standard chemical protocol followed in experiments. Rather, it is designed for describing the overall structure of the particles, independently of the followed procedure. For the case being, this does not translate into having specific particles with the role of "initiator" in the computational synthesis. Rather, the focus is centered to the effect that the addition of initiator at different times has on the final structure, and thus on crosslinker distribution, of the individual microgels. Specifically, here we find that two parameters in the computational synthesis are particularly relevant for reproducing correctly the microgel architecture obtained experimentally upon changing t_{add}, namely the size of the core compared to the overall size of the particle and the ratio between the number of monomers among different microgel batches, as discussed in more detail in the following.

3.2.1 Setting the number of monomers. In order to determine the relative number of monomers belonging to each microgel, we exploit the viscosity measurements whose results are summarized in Fig. 2. In fact, the knowledge of k allows us to extract the proportionality constant between the microgel effective packing fraction ϕ_{eff} and their weight concentration C_w, which reads as,[26,34]

$$k = \frac{\phi_{eff}}{C_w} = \frac{N_m V_m}{V}\frac{V}{M} = \frac{N_m V_m}{M} \tag{15}$$

where N_m is the number of microgels in the suspension, V_m the volume of each microgel, V the total volume of the suspension, M the total mass of monomer. We can then calculate the ratio

$$\frac{k^{t_{add},i}}{k^{t_{add},j}} = \frac{N_m^{t_{add},i} V_m^{t_{add},i}}{N_m^{t_{add},j} V_m^{t_{add},j}} = \frac{N_m^{t_{add},i}\left(R_m^{t_{add},i}\right)^3}{N_m^{t_{add},j}\left(R_m^{t_{add},j}\right)^3}, \tag{16}$$

where R_m is the radius of the microgels, and $t_{add,(i,j)}$ indicates the initiator addition time of batch i or j. Since both k and R_m are known from experiments, we can now invert the relation and calculate the number of microgels in each batch as,

$$\frac{N_m^{t_{add},i}}{N_m^{t_{add},j}} = \frac{k_{t_{add},i}}{k_{t_{add},j}}\frac{\left(R_m^{t_{add},j}\right)^3}{\left(R_m^{t_{add},i}\right)^3}. \tag{17}$$

Using the experimental values, we finally have,

$$N_m^{t_{add}=0.2} \approx 0.7 N_m^{t_{add}=1} \approx 0.5 N_m^{t_{add}=9}, \tag{18}$$

with N_m being inversely proportional to the number of monomers N for each microgel at a fixed total mass M. In the modeling, we thus take this into account in order to reproduce the correct size dependence observed in the synthesis and

assemble microgels with a different nominal number of monomers N. In particular, fixing $N^{t_{add}=9} \approx 168k$, we obtain $N^{t_{add}=1} \approx 230k$ and $N^{t_{add}=0.2} \approx 336k$. For convenience, we name such microgels M_s, M_m and M_l, to indicate their small, medium and large size, for an increasing N, as also summarised in Table 1. We recall that the actual number of monomers incorporated in the microgels after the assembly is usually slightly different than the nominal one. Importantly, this analysis already gives an indication of how the formation of microgels occurs during the experimental synthesis, suggesting that in case the initiator is added all at once, the polymerisation process is concentrated in a smaller number of nucleation centers with more monomers each. On the contrary, a slower inclusion of KPS over time allows for the formation of a larger amount of nuclei, each composed by a smaller amount of monomers.

3.2.2 Setting the core-to-corona ratio. Microgels with a different core-to-corona ratio show different topologies and related form factors. To study this effect, we assemble microgels with a fixed number of monomers N and varying ratio between the core C and the overall microgel Z radii, at fixed Z. Here, we consider M_l microgels with $0.5 \leq C/Z \leq 0.8$ at fixed $Z = 100\sigma$ in order to better visualize changes between the different C employed. The value of the core radius is placed as apex of each microgel name, see Table 1. Representative simulation snapshots showing the full particles and the corresponding microgel slices are displayed in Fig. 4, highlighting the reduction in size of the core as C/Z decreases. The respective form factors $P(q)$ are reported in Fig. 5(a), arbitrarily shifted on the y-axis for the sake of visual clarity.

Although the number of monomers is fixed, the microgels exhibit a slight increase in total size as the core size decreases, as indicated by distance where the radial density profile approaches zero (inset in Fig. 5(b)). The position of the first peak of $P(q)$ remains roughly constant, which is an indication that the radius of gyration of the microgels is also quite constant (not shown). This observation is not in contradiction with the increase in total size, as for smaller cores, the particle becomes denser toward its center and the overall extension of the particle can still be larger, driven by the presence of a less dense, but more extended corona. Indeed, the structure and extension of the corona change, as evidenced by the appearance of two distinct gradient regions in the radial density profiles. These correspond to the shift, toward higher wavenumbers of the second and third peaks in the form factors for the M_l^{c60} and M_l^{c50} samples reported in Fig. 5(a).

This picture suggests that if the crosslinkers are concentrated in a larger and larger volume, the overall size of the particle tends to be smaller than for the opposite case, where a more spread and swollen structure is retained. This is confirmed by the radial density profiles $\rho(r)$ shown in Fig. 5(b), which provide the same information in real space but allowing for a better visualization of the variation of the core size with C. In addition, the inset shows that the smaller the core, the greater the long-distance tail of the profiles, indicating the growing size of the particles. These results can also be visually detected by looking at the snapshots of the corresponding microgels, where an overall fluffier structure with longer outer chains is consistently observed for microgels with a smaller core.

3.3 Comparison between *in silico* microgels and experiments

By combining the information derived in the previous sections, it is now possible to obtain detailed models for each of the

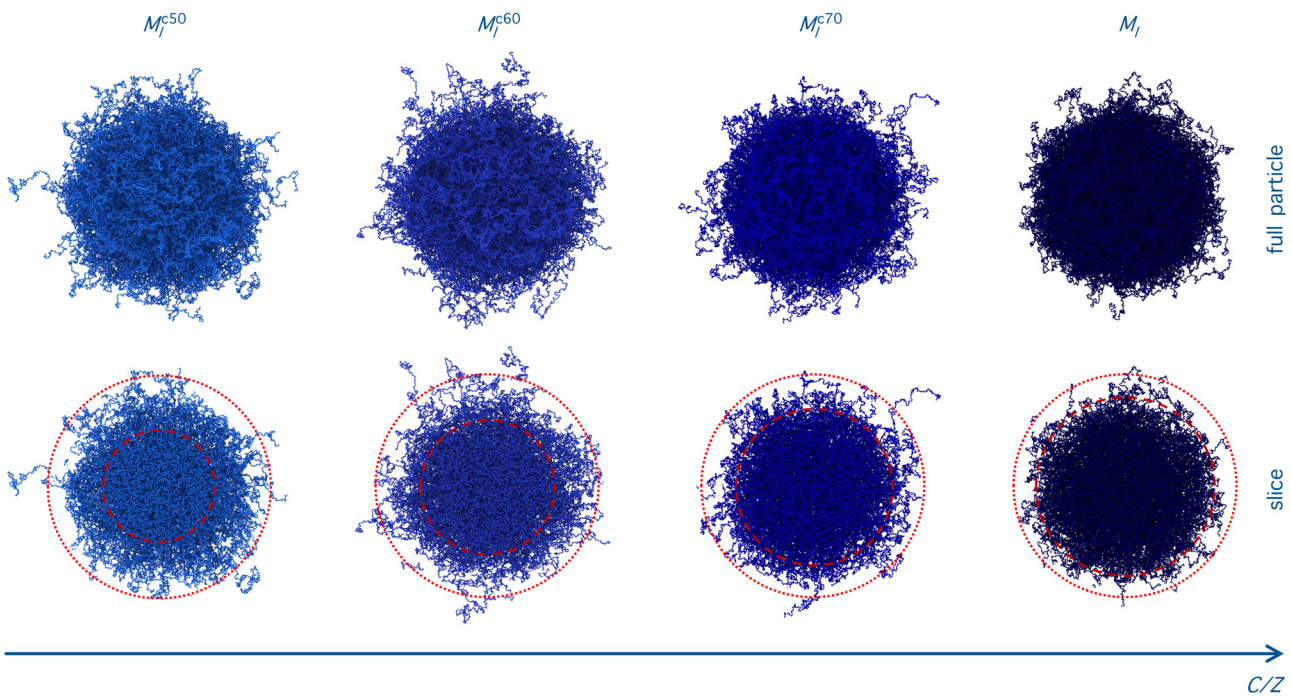

Fig. 4 Representative simulation snapshots showing the (top row) full and (bottom row) sliced M_l^{c50}, M_l^{c60}, M_l^{c70} and M_l microgels (from left to right) with different core to microgel assembly radii C/Z. Dotted and dashed lines show the nominal particle and core radius, Z and C, respectively.

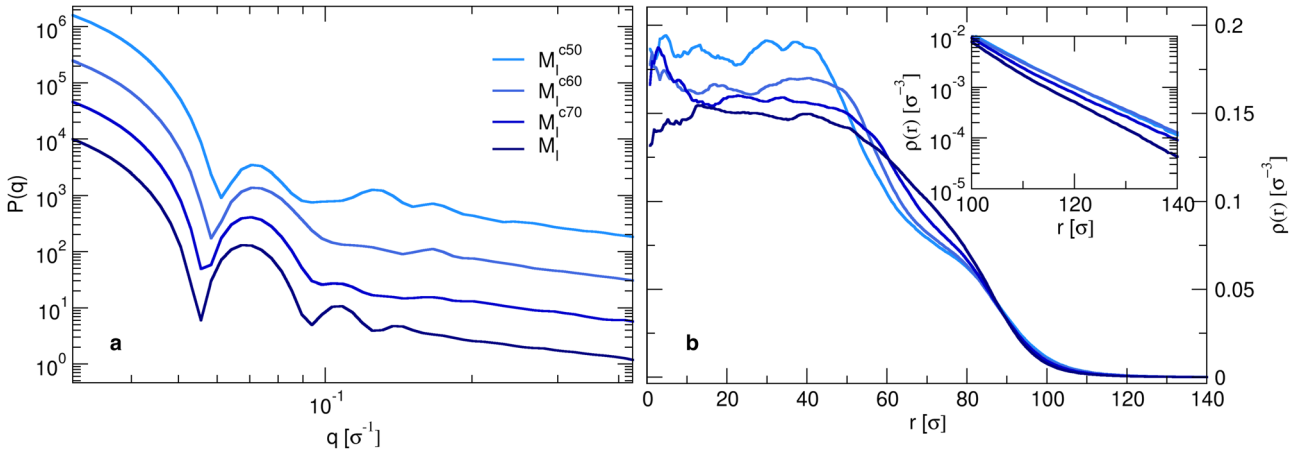

Fig. 5 (a) Numerical form factors $P(q)$ as a function of the wavenumber q and (b) corresponding radial density profiles as a function of the distance r for the M_l^{c50}, M_l^{c60}, M_l^{c70} and M_l *in silico* microgels. Inset: Zoom on the long distance tail of the radial density profile.

synthesized batches. In order to do so, it is straightforward to compare the $I_m(q)$ derived from the analysis of the experimental data to the form factors calculated numerically. The determination of the $I_m(q)$ data is reported in the Methods section. In order to determine the conversion unit between simulations and experiments, we superimpose the first peak of the numerical form factor onto the experimental one at the lowest investigated temperature.[12] Then, the same scaling factor, corresponding to the measure of the bead size σ used in simulations, is retained for all other temperatures.

Experimental and numerical form factors for initiator addition times of 0.2,1.0 and 9.0 minutes are shown with symbols and full lines, respectively, in Fig. 6(a) for T = 293 K and in Fig. 6(b) for 313 K. The numerical form factors are calculated for microgels M_l, M_m and M_s, as discussed in the previous section, in order to account for the smaller amount of monomers present in each of the experimental microgels for longer t_{add}. The size of the core C is here adjusted as the main fit parameter for matching at best the experimental measurements. A remarkable agreement with the experiments is obtained for a progressively smaller size of the core as the initiator addition time increases. Correspondingly, the ratio between the core and the microgel radii C/Z also decreases, going from around 0.8 to 0.65 from 0.2 to 9 minutes of initiator addition time. These findings are in qualitative agreement with the analysis of the neutron scattering data, showing that the core extension decreases as t_{add} increases, as reported in Table S2 (ESI†). It is important to note that the same microgel model is also able to reproduce the form factors of the surfactant-free microgel for t_{add} = 9 minutes, as reported in Fig. S1 (ESI†). This reassures us that the model is robust toward size effects, independently on the internal microgel architecture. Referring back to Fig. 3, it is evident that the form factors exhibit a shift of the first peak towards higher wavenumbers as t_{add} increases, consistent with a reduction in the size of the particles. Besides, we also note a progressive disappearance of the second peak of the form factors in the swollen state that becomes almost invisible for the smallest microgels. The deviations between numerical and experimental form factors found at

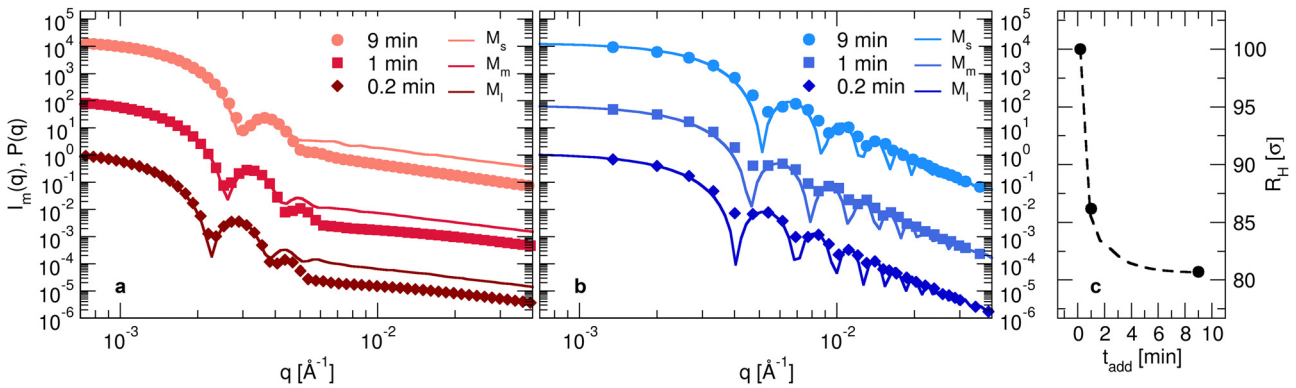

Fig. 6 Model scattering intensity $I_m(q)$ (symbols) as a function of the wavenumber q obtained from the analysis of SANS data on PNIPAM microgels synthesised with KPS added in 0.2, 1 and 9 min at 293 K and 313 K. Also shown are numerical form factors $P(q)$ calculated from molecular dynamics trajectories (lines) for M_l(C = 0.80Z), M_m(C = 0.75Z) and M_s(C = 0.65Z). Data are reported for (a) T = 293 K and (b) T = 313 K. Simulations data are shifted by the common factor 2.45 nm that is the size of the bead used in the model. (c) Hydrodynamic radius R_H as a function of initiator addition time t_{add}, that is for M_l, M_m and M_s microgels, respectively, in the swollen state. The dashed line serves as guide-to-the-eye.

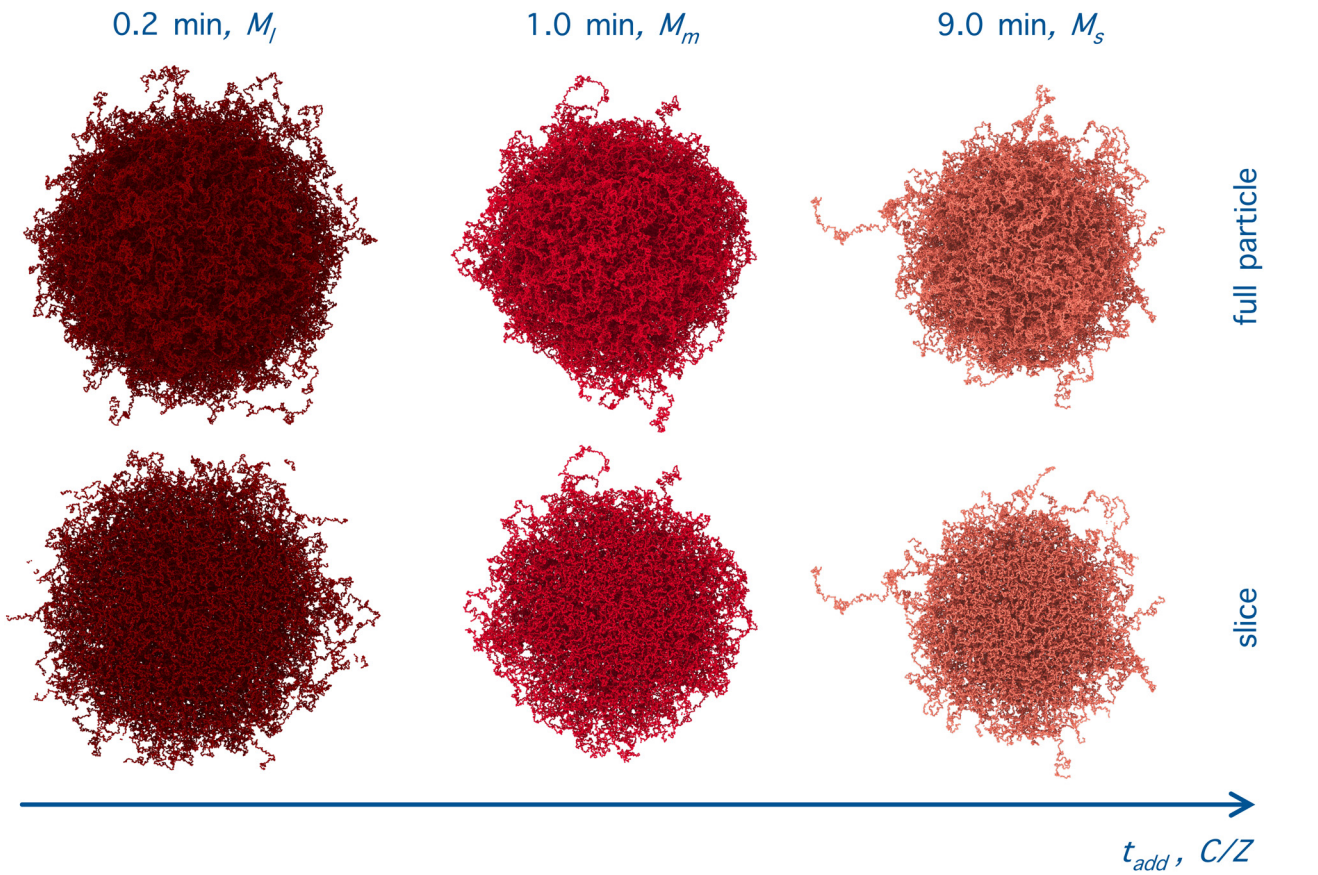

Fig. 7 Representative simulation snapshots showing the (top row) full and (bottom row) sliced M_l, M_m, and M_s microgels (from left to right), with different number of monomers N and core-to-microgel radii ratio C/Z, corresponding to different experimental initiator addition times t_{add}.

high wavenumbers are a consequence of the finite size of the beads for *in silico* microgels as compared to the actual laboratory ones.[12] The situation improves at high temperatures, where we observe many characteristic oscillations of a fully collapsed spherical microgel network.

Importantly, the present modeling is also able to reproduce the experimental trend of hydrodynamic radius R_H observed in the experiments. This quantity, calculated from molecular dynamics trajectories of single microgels as described in Methods, is shown in Fig. 6(c) for the cases under investigation. Consistently with DLS results (Fig. 1(a)), we find that R_H of the simulations significantly drops from the value it retains at the smallest initiator addition time to the intermediate one (at 1 minute), and then slightly decreases further when KPS addition occurs over 9 minutes. The relative decrease in R_H is also in qualitative agreement with DLS experiments, showing a first reduction by around 15% and a subsequent one by another 5–10%. The change in size of the investigated microgels can also be visualized by means of the simulation snapshots reported in Fig. 7.

4 Conclusions

In this work, we analyzed in detail the modifications of the microgel conformation upon changing the time in which the initiator is added to the standard chemical synthesis. Variations at this stage in the protocol are expected to influence the distribution of the crosslinkers within microgel particles and, in turn, the overall microgel architecture. Despite being a small variation in the synthesis procedure, the importance of this study stems from the fact that in the literature microgels are prepared almost interchangeably with either the addition of the initiator in one-shot (low t_{add}) or with the drop-by-drop (high t_{add}) protocol. This variation of the synthesis protocol determines subtle changes in the observed microgel structure, previously undocumented, thus requiring a careful modeling effort.

Therefore, the present work analyzes the effect of initiator addition time by combining experiments and simulations. Our findings show a non-trivial phenomenology. First of all, we find that a fast addition time results in microgels having a larger core with respect to the total size of the network, hence denoting a more homogeneous structure. Instead, a longer addition time yields a more marked difference between core and corona and thus microgels with a more heterogeneous network. To model this in simulations, we use a more compact distribution of crosslinkers and thus a smaller core radius, which naturally yields a more stretched corona. On the other hand, an almost instantaneous addition of the initiator gives rise to a large core, as also confirmed by simulations. Interestingly, it is the first type of microgels—the more heterogeneous

one in terms of core–corona structure—to be larger in size according to DLS, while the second ones are significantly smaller.

To shed light on these interesting features, we analysed the experimental synthesis in terms of the number of microgel nuclei that are formed during the polymerisation reaction, which is found to vary significantly with the addition time of the initiator. This was indirectly observed by means of viscosity measurements in dilute conditions. By combining all these elements together, it was possible to capture the evolution of the microgel structure with different initiator addition times, which results from two distinct contributions. On the one hand, there is a tendency for the microgels to become more and more heterogeneous in terms of core–corona ratio as t_{add} increases and, on the other hand, we observe a decrease in microgel size due to a reduced capacity to incorporate monomers within the network. Although it might be expected that a slower addition would result in a more homogeneous structure, this is not confirmed by the data. Actually, it is the microgels with the initiator added all at once to have a larger core with respect to the corona, and thus being overall more homogeneous. However, this results in fewer microgel nuclei being generated, which has a significant impact on the polymerisation process. In this respect, it would be interesting to monitor the kinetics of reaction for the formation of these particles. In addition, attenuation studies similar to those recently performed in ref. 35, could be valuable to confirm the present results.

It is important to note that the present findings are obtained with the complementary addition of a fixed amount of surfactant. Nonetheless, we have repeated the synthesis in its absence for the case of initiator addition time of 9 minutes, and we found no substantial differences. The corresponding form factors, reported in the ESI,† are also captured by the numerical model with the same core-to-corona ratio as for the smaller experimental microgels. Hence, we can conclude that the current findings do not appear to be affected by the presence of surfactant in the experimental synthesis.

In summary, we have shown that the addition of the initiator at different times has relevant effects on the polymerization process of microgels, and can be exploited for fine-tuning the particles internal architectures and sizes. These findings are found to be independent on the use of surfactants in the synthesis protocol and thus unaffected by microgel size. This provides a straightforward, additional parameter in the experimental synthesis, enabling the optimization of microgel preparation for specific applications. In the future, it will be interesting to extend this study to different types of microgels, also based on different monomeric units, such as PVCL,[36] and crosslinking agents,[37,38] in order to investigate how these factors influence the internal structure. By combining experimental and simulation approaches, future work could aim to identify conditions that promote either maximal structural homogeneity or inhomogeneity, further advancing the understanding of microgel design.

Author contributions

E. B. and F. C. contributed equally to this work. Conceptualization: E. Z.; formal analysis: E. B., F. C., V. N., S. F., Y. G., E. Z.; funding acquisition: E. Z.; investigation: E. B., F. C., V. N., S. F., J. R.-F., Y. G., E. Z.; methodology: Y. G., E. Z.; project administration: E. Z.; software: Y. G.; supervision: R. A., B. R., E. Z.; validation: F. C., V. N., Y. G., E. Z.; visualization: F. C.; writing – original draft: F. C., Y. G., E. Z.; writing – review and editing: E. B., F. C., V. N., S. F., J. R.-F., L. P., R. A., B. R., Y. G., E. Z.

Data availability

Data for this article are available on the online repository Zenodo (**https://doi.org/10.5281/zenodo.14267285**). SANS experimental data can be accessed at **https://doi.ill.fr/10.5291/ILL-DATA.EASY-1060**.

Conflicts of interest

There are no conflicts to declare.

Acknowledgements

We dedicate this manuscript to the memory of our colleague Stefan Egelhaaf, a great scientist and a dear friend. We are deeply grateful for the fruitful collaborations and interactions we had with him throughout the years. We also thank Giovanni Del Monte for sharing the code for the calculation of the hydrodynamic radius in simulations and Andrea Ninarello for useful discussions. We thank the Institut Laue – Langevin for the awarded neutron beamtime (doi: **https://doi.org/10.5291/ILL-DATA.EASY-1060**). This work benefited from the use of the SasView application, originally developed under NSF award DMR-0520547. SasView contains code developed with funding from the European Unions Horizon 2020 research and innovation programme under the SINE2020 project, grant agreement no. 654000. EB and EZ acknowledge financial support by the Italian Ministry of University and Research (MUR) under the National Recovery and Resilience Plan (NRRP), Mission 4, Component 2, Investment 1.1, Call for tender no. 104 published on 2.2.2022 by the Italian Ministry of University and Research (MUR), funded by the European Union – NextGenerationEU-Project Co-MGELS, contract nr. 2022PAYLXW.

Notes and references

1 Z. Zhang, N. Xu, D. T. Chen, P. Yunker, A. M. Alsayed, K. B. Aptowicz, P. Habdas, A. J. Liu, S. R. Nagel and A. G. Yodh, *Nature*, 2009, **459**, 230–233.
2 D. Paloli, P. S. Mohanty, J. J. Crassous, E. Zaccarelli and P. Schurtenberger, *Soft Matter*, 2013, **9**, 3000–3004.
3 P. J. Yunker, K. Chen, M. D. Gratale, M. A. Lohr, T. Still and A. Yodh, *Rep. Prog. Phys.*, 2014, **77**, 056601.
4 G. Del Monte and E. Zaccarelli, *Phys. Rev. X*, 2024, **14**, 041067.

5 M. Karg, A. Pich, T. Hellweg, T. Hoare, L. A. Lyon, J. Crassous, D. Suzuki, R. A. Gumerov, S. Schneider and I. I. Potemkin, *et al.*, *Langmuir*, 2019, **35**, 6231–6255.
6 J. Brijitta and P. Schurtenberger, *Curr. Opin. Colloid Interface Sci.*, 2019, **40**, 87–103.
7 S. Kumari, M. Avais and S. Chattopadhyay, *ACS Appl. Polym. Mater.*, 2023, **5**, 1626–1645.
8 J. Zheng, C. Zhu, X. Xu, X. Wang and J. Fu, *J. Mater. Chem. B*, 2023, **11**, 6265–6289.
9 R. Pelton, *Adv. Colloid Interface Sci.*, 2000, **85**, 1–33.
10 A. Fernandez-Nieves, H. Wyss, J. Mattsson and D. A. Weitz, *Microgel suspensions: fundamentals and applications*, John Wiley & Sons, 2011.
11 M. Stieger, W. Richtering, J. S. Pedersen and P. Lindner, *J. Chem. Phys.*, 2004, **120**, 6197–6206.
12 A. Ninarello, J. J. Crassous, D. Paloli, F. Camerin, N. Gnan, L. Rovigatti, P. Schurtenberger and E. Zaccarelli, *Macromolecules*, 2019, **52**, 7584–7592.
13 E. Mueller, R. J. Alsop, A. Scotti, M. Bleuel, M. C. Rheinstädter, W. Richtering and T. Hoare, *Langmuir*, 2018, **34**, 1601–1612.
14 T. Kyrey, J. Witte, A. Feoktystov, V. Pipich, B. Wu, S. Pasini, A. Radulescu, M. U. Witt, M. Kruteva and R. von Klitzing, *et al.*, *Soft Matter*, 2019, **15**, 6536–6546.
15 O. Virtanen, A. Mourran, P. Pinard and W. Richtering, *Soft Matter*, 2016, **12**, 3919–3928.
16 G. Del Monte, D. Truzzolillo, F. Camerin, A. Ninarello, E. Chauveau, L. Tavagnacco, N. Gnan, L. Rovigatti, S. Sennato and E. Zaccarelli, *Proc. Natl. Acad. Sci. U. S. A.*, 2021, **118**, e2109560118.
17 S. Sennato, E. Chauveau, S. Casciardi, F. Bordi and D. Truzzolillo, *Polymers*, 2021, **13**, 1153.
18 N. Gnan, L. Rovigatti, M. Bergman and E. Zaccarelli, *Macromolecules*, 2017, **50**, 8777–8786.
19 N. Hazra, A. Ninarello, A. Scotti, J. E. Houston, P. Mota-Santiago, E. Zaccarelli and J. J. Crassous, *Macromolecules*, 2023, **57**, 339–355.
20 B. J. Frisken, *Appl. Opt.*, 2001, **40**, 4087–4091.
21 J. W. White, *Proc. R. Soc. London, Ser. A*, 1975, **345**, 119–143.
22 C. D. Dewhurst, *J. Appl. Crystallogr.*, 2023, **56**, 1595–1609.
23 *SasView*, **https://www.sasview.org/**.
24 H. A. Barnes, in *Rheology: Principles, Measurements and Applications*, ed. C. W. Macosko, published by VCH Publishers, Weinheim, Germany, 1996, p. 550.
25 G. K. Batchelor, *J. Fluid Mech.*, 1977, **83**, 97–117.
26 H. Senff and W. Richtering, *J. Chem. Phys.*, 1999, **111**, 1705–1711.
27 S. Franco, E. Buratti, B. Ruzicka, V. Nigro, N. Zoratto, P. Matricardi, E. Zaccarelli and R. Angelini, *J. Phys.: Condens. Matter*, 2021, **33**, 174004.
28 L. Rovigatti, P. Šulc, I. Z. Reguly and F. Romano, *J. Comput. Chem.*, 2015, **36**, 1–8.
29 J. D. Weeks, D. Chandler and H. C. Andersen, *J. Chem. Phys.*, 1971, **54**, 5237–5247.
30 H. R. J. Warner, *Ind. Eng. Chem. Fundam.*, 1972, **11**, 379–387.
31 T. Soddemann, B. Dünweg and K. Kremer, *Eur. Phys. J. E: Soft Matter Biol. Phys.*, 2001, **6**, 409–419.
32 A. P. Thompson, H. M. Aktulga, R. Berger, D. S. Bolintineanu, W. M. Brown, P. S. Crozier, P. J. in 't Veld, A. Kohlmeyer, S. G. Moore, T. D. Nguyen, R. Shan, M. J. Stevens, J. Tranchida, C. Trott and S. J. Plimpton, *Comput. Phys. Commun.*, 2022, **271**, 108171.
33 J. B. Hubbard and J. F. Douglas, *Phys. Rev. E: Stat. Phys., Plasmas, Fluids, Relat. Interdiscip. Top.*, 1993, **47**, R2983.
34 R. Elancheliyan, G. Del Monte, E. Chauveau, S. Sennato, E. Zaccarelli and D. Truzzolillo, *Macromolecules*, 2022, **55**, 7526–7539.
35 M. Otten, M. Hildebrandt, B. Pfeffing, V. C. Voigt, F. Scheffold, T. Hellweg and M. Karg, *Langmuir*, 2024, **40**, 14515–14526.
36 F. Schneider, A. Balaceanu, A. Feoktystov, V. Pipich, Y. Wu, J. Allgaier, W. Pyckhout-Hintzen, A. Pich and G. J. Schneider, *Langmuir*, 2014, **30**, 15317–15326.
37 K. Kratz, A. Lapp, W. Eimer and T. Hellweg, *Colloids Surf., A*, 2002, **197**, 55–67.
38 J. Ruiz-Franco, R. Rivas-Barbosa, M. A. Lara-Peña, J. R. Villanueva-Valencia, A. Licea-Claverie, E. Zaccarelli and M. Laurati, *Soft Matter*, 2023, **19**, 3614–3628.